Journal of
Materials Chemistry A

PAPER

View Article Online
View Journal | View Issue

Check for updates

Cite this: *J. Mater. Chem. A*, 2023, **11**, 15204

Received 7th April 2023
Accepted 23rd June 2023

DOI: 10.1039/d3ta02115g

rsc.li/materials-a

Metal-support interactions alter the active species on IrO_x for electrocatalytic water oxidation†

Ge-Yang Xu,[a] Mu-Fei Yue,[a] Zheng-Xin Qian,[a] Zi-Yu Du,[a] Xiao-Qun Xie,[a]
Wei-Ping Chen,[ab] Yue-Jiao Zhang *[a] and Jian-Feng Li *[abc]

Constructing metal-support interaction (MSI) is a strategy of wide interest to promote the electrocatalytic performance of oxygen evolution reaction (OER). However, studies helping to understand the electrocatalytic behavior of reactive centers affected by the metal support and investigations to guide the construction of catalysts based on MSI are scarce. *In situ* surface-enhanced Raman spectroscopy (SERS) provides spectral evidence of reactive intermediates and information on the structural evolution of catalysts, which can help investigate the reaction pathway of catalysts. In this work, Au@MnO_2-IrO_x core–shell nanoparticles (NPs), possessing a specific nanostructure of highly dispersed IrO_x clusters on amorphous MnO_2 shells, were prepared by a simple method under ambient conditions and exhibited a low overpotential of 230 mV to reach the current density of 10 mA cm^{-2}, therefore outperforming the traditional Ir catalysts. The oxidation of Ir^{4+} and adsorption of *O on IrO_x at a low potential were revealed by *in situ* SERS, which indicated the pre-activation of Ir centers and the facilitated formation of superoxide species: *O–O$^-$. Combined with density functional theory (DFT) calculations, we show that the MnO_2 substrate optimizes binding energies of intermediates on IrO_x, promoting O–O coupling and improving the OER rate. This work provides a strategy for utilizing *in situ* spectroscopy to investigate the OER mechanism and understand the electrocatalytic behavior impacted by MSI.

1. Introduction

As an environment-friendly way of hydrogen production, electrocatalytic water splitting offers a promising way to mitigate the energy and environmental crisis.[1–3] The anodic oxygen evolution reaction (OER) is a half-reaction of the water splitting. It is a four-electron transfer reaction that is more kinetically sluggish than the cathodic hydrogen evolution reaction (HER).[3–5]

Although great efforts have been invested to develop OER catalysts, non-noble metal-based catalysts still underperform the benchmarks of Ru-based and Ir-based catalysts. Ru is supposed to be a prospective candidate for Ir because of its higher abundance on earth, lower price, and even better OER activity.[6,7] However, Ru-based catalysts show inferior stability, limiting their further application.[8] So far, Ir is still the most suitable OER catalyst.

For the usage of Ir reasonably, designing Ir-based nanocatalysts to improve the Ir atom utilization is a promising route to replace the classical IrO_2 bulk catalysts.[9] For example, some

Yue-Jiao Zhang obtained her PhD in chemistry from the College of Chemistry and Chemical Engineering, Xiamen University, in 2020. She is currently an assistant professor at the College of Energy, Xiamen University. Her present research interests focus on plasmonic core–shell nanomaterials, surface-enhanced Raman spectroscopy (SERS), in situ spectroscopies for electrocatalysis, and rapid Raman detection. She has published more than 50 papers, including in Nat. Rev. Methods Primers, J. Am. Chem. Soc., Angew. Chem. Int. Ed., Adv. Mater., ACS Nano, Small Methods, Nano Lett., and Anal. Chem.

---

[a] College of Energy, State Key Laboratory of Physical Chemistry of Solid Surfaces, iChEM, College of Chemistry and Chemical Engineering, College of Materials, Xiamen University, Xiamen 361005, China. E-mail: zhangyuejiao@xmu.edu.cn; li@xmu.edu.cn

[b] Innovation Laboratory for Sciences and Technologies of Energy Materials of Fujian Province (IKKEM), Xiamen 361005, China

[c] College of Optical and Electronic Technology, China Jiliang Unversity, Hangzhou 310018, China

† Electronic supplementary information (ESI) available. See DOI: https://doi.org/10.1039/d3ta02115g

cases introduce new metal components, such as Ru, Au, Ta, Tm,[10–12] *etc.*, which modify the surface electronic structure and generate certain ligand or synergistic effects to modulate the adsorption of reactive intermediates, thus improving the catalytic performance.[13]

Recently, constructing a strong metal-support interaction (SMSI) has garnered great attention. SMSI may modulate the catalytic performance to a great extent, whereby metal catalysts are downsized into nanoparticles, nanoclusters, and even single atoms and are anchored on the support material.[14–17] On one hand, electron transfer may occur between the metal catalyst and support, changing the local electronic structure of metal catalysts. On the other hand, metal nanostructures anchored on the support may have a specific atomic coordination environment and possess distinct structure deformation.[16,18] For example, IrO_2 clusters were embedded in the porous network of V_2O_5 to form highly dispersed IrO_2/V_2O_5 catalysts.[19] Charges transferred from IrO_2 to V_2O_5, and then the IrO_2 clusters served as the electrophilic centers to promote the hydroxyl oxidation kinetics and the O–O bond coupling process, eventually accelerating the OER rate. In another work, atomically dispersed Ir active sites were anchored into a hetero-nitrogen-configured carbon substrate and formed AD-HN-Ir electrocatalysts with active hetero-Ir-N_4 nanostructures.[20] Coupled Ir centers with high valence could pre-adsorb oxygen atoms and accelerate the formation of key intermediates *OOH. Recently, MnO_2 as the support to improve the catalytic activity of reactive centers has attracted growing interest, because various valence states and crystalline phases of manganese oxides can result in varying surface electronic and coordination structures.[21–23] However, studies to understand the electrocatalytic behavior of reactive centers impacted by the support remain scarce.

Relying on its high sensitivity and detection superiority in the low-wavenumber region, surface-enhanced Raman spectroscopy (SERS) has attracted much attention.[24–27] SERS, when applied to monitor the electrocatalytic reaction, can gain information on not only reactive intermediates, such as oxygen species, hydroxyl group *et al.*,[28–30] but also the structural evolution of electrocatalysts with the change in electrode potential,[31,32] helping reveal the OER pathway and synergies between metal centers and support.

In this work, Au@MnO_2-IrO_x NPs were constructed based on the "borrowing" strategy.[27,33] Au cores could amplify the Raman signal of species adsorbed on the shells. Ir oxide catalysts (IrO_x) were anchored on amorphous MnO_2 shells with high dispersion; strong electronic interaction existed with the charge transfer from IrO_x to MnO_2. In the electrochemical measurements, Au@MnO_2-IrO_x NPs delivered a low overpotential of 230 mV (10 mA cm^{-2}) with an ultra-high mass activity, thus outperforming the Au@Ir NPs and commercial IrO_2 catalysts. *In situ* SERS demonstrated the pre-activation of Ir reactive centers at a low potential, which facilitated the formation of superoxide species: *O–O^-. The density functional theory (DFT) calculations clarified that the MnO_2 substrate could weaken the energy barriers of the O–O coupling and deprotonation of *OOH on the Ir oxide, which boosted the OER activity.

2. Experimental section

2.1 Preparation of 55 nm Au NPs

Au NPs were prepared according to the reported Fren's method.[34] Here, 2.424 mL of 1% $HAuCl_4\cdot 4H_2O$ solution was added to 200 mL of de-ionized (DI) water. The solution was heated until it boiled, and 1.5 mL of 1% sodium citrate solution was quickly injected under vigorous stirring. The color of the system changed from faint yellow to brick red in a few minutes, indicating ~55 nm Au NPs colloid was successfully synthesized. The heat and stirring should be maintained for at least half an hour to ensure the completeness of the reaction. Then, the system was cooled to ambient temperature naturally.

2.2 Preparation of Au@Ir NPs

To prepare Au@Ir NPs, 30 mL of the Au NPs colloid prepared above and 2.5 mL of 1% sodium citrate solution were mixed and heated to a boil. 5 mL of 1 mM $IrCl_3$ solution were gradually injected under vigorous stirring. Half an hour was allowed to complete the reaction. At last, the colloid, through natural cooling, was centrifuged and washed twice.

2.3 Preparation of Au@MnO_2 with ~3 and ~8 nm shell NPs

Au@MnO_2 NPs were synthesized referring to the reported method.[35] 10 mL of the Au NPs colloid was cooled to 4 °C in the ice bath, followed by injection of 170 μL of 0.1 M KOH solution and 0.5 mL of 10 mM $KMnO_4$ solution with stirring. 2.5 mL of 10 mM $K_2C_2O_4$ solution were dropped into the system gradually. The reaction mixture was stirred in the ice bath for 2 hours, which produced Au@3 nm MnO_2 NPs. To acquire Au@8 nm MnO_2 NPs, the colloid had to be transferred to a 60 °C-water bath for 3 hours. At last, the colloids were centrifuged and washed twice.

2.4 Preparation of Au@MnO_2-IrO_x NPs

Au@MnO_2-IrO_x NPs were fabricated by the impregnation method. The Au@MnO_2 colloids were dispersed in 10 mL of DI water, followed by the addition of 400 μL of 1 mM $IrCl_3$ solution. The system was stirred for 3 h at ambient temperature. Afterward, 50 μL of 10 mM $NaBH_4$ solution was injected slowly. At last, the colloid was centrifuged and washed twice.

2.5 Characterizations

The morphology and elemental mapping analysis of samples were performed by FEI Tecnai F30 and JEM-1400 microscopes. X-ray photoelectron spectroscopy was performed using Thermo Scientific ESCALAB Xi+. Inductively coupled plasma-optical emission spectrometry (ICP-OES) was performed using SPECTRO SPECTROBLUE FMX36. X-ray diffraction (XRD) patterns were acquired using Rigaku Ultima IV.

2.6 Electrochemistry

All tests were performed in a three-electrode system under ambient pressure with an electrochemical workstation (CHI 760E). The sample coated on the disk electrodes (0.196 cm^2) was used as the working electrode, and the Pt wire and the mercuric oxide (Hg/HgO) electrode were used as the counter and reference electrodes, respectively. 1 M KOH saturated with O_2 was used as the electrolyte. A sample slurry was prepared by the following method: 5 mg of catalyst and 1 mg of carbon black were dispersed in 400 μL of an alcohol/water solution (volume ratio, 1 : 1) and 10 μL of 5% Nafion; the slurry was then sonicated for half an hour for later measurements.

2.7 *In situ* electrochemical Raman measurements

Raman confocal microscope Raman system Xplora (HORIBA Jobin Yvon) was used to acquire Raman spectra. The excitation wavelength of the He–Ne laser was 638 nm, and a 50× microscope objective was used. The Raman frequencies were calibrated using a Si wafer (520.6 nm) before each Raman experiment. *In situ* electrochemical Raman experiments were carried out in the homemade Raman cell with a three-electrode system: the glass carbon electrode as the working electrode, Pt wire as the counter electrode, and Hg/HgO electrode as the reference electrode. The applied potential was controlled by the potentiostat from Xiamen Qunji Instrument Co. Ltd. Raman spectra were acquired under the potential range of 1.20–1.70 V (*vs.* RHE), and 30 s at least should be paid before acquiring each Raman spectrum.

3. Results and discussion

The synthetic route for preparing Au@MnO_2 NPs is described in the Experimental section. Transmission electron microscopy (TEM) showed the morphology of Au@MnO_2 with a ∼55 nm Au core to be covered by a smooth shell of ∼3 nm (Fig. S3a†). Only the typical Au diffraction peaks and no lattice fringes were shown by the X-ray diffraction (XRD) patterns (Fig. S4a†) and high-resolution transmission electron microscope (HRTEM)

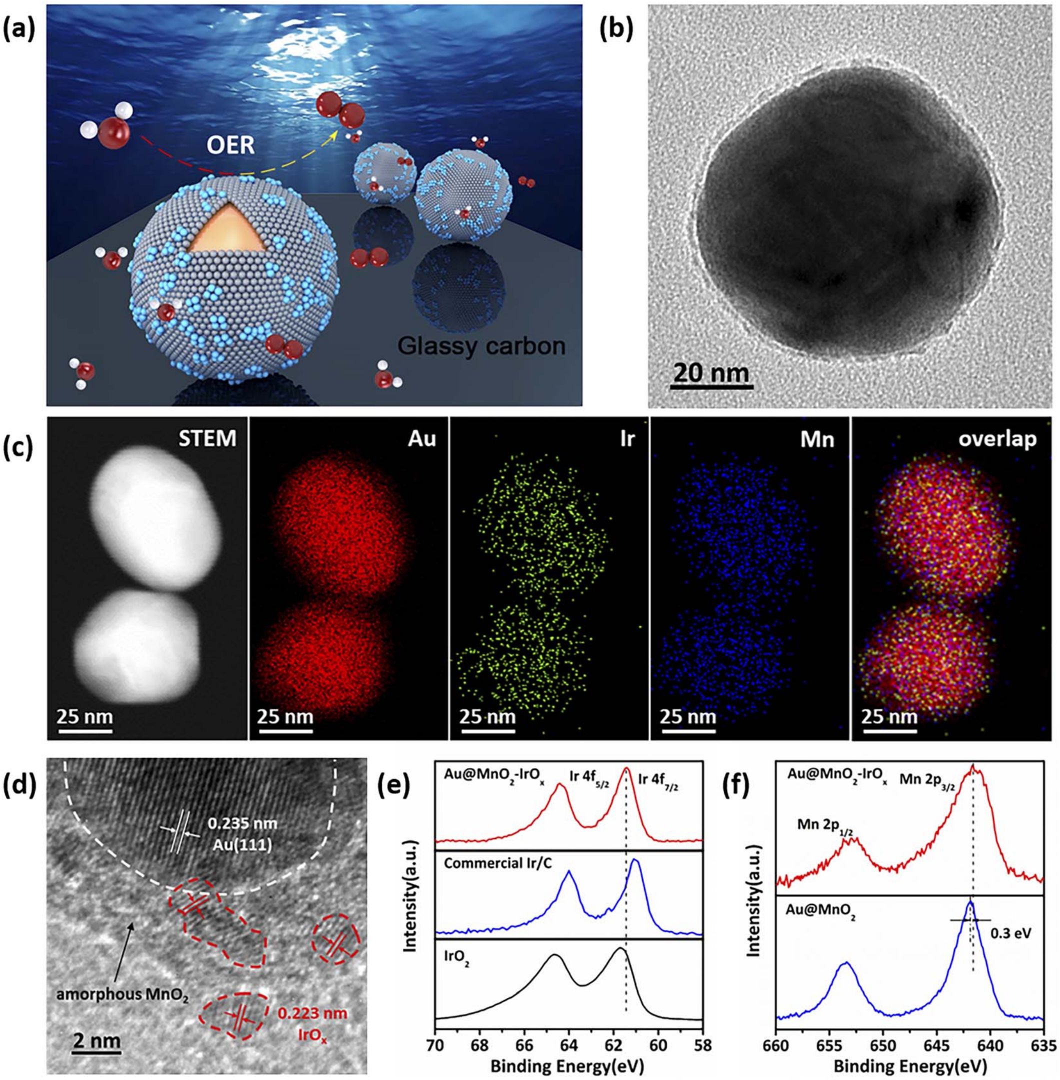

Fig. 1 (a) Schematic illustration of Au@MnO_2-IrO_x core–shell nanoparticle-enhanced Raman spectroscopy for *in situ* electrochemical study. (b) TEM image of Au@MnO_2-IrO_x NPs. (c) Elemental mapping images of Au@MnO_2-IrO_x NPs. (d) HRTEM image of the Au@MnO_2-IrO_x-a NPs. (e) The Ir 4f XPS spectra of Au@MnO_2-IrO_x NPs. (f) The Mn 2p XPS spectra of Au@MnO_2-IrO_x NPs.

images (Fig. S4b†), respectively, indicating that MnO_2 shells were amorphous. The Raman spectra of Au@8 nm MnO_2 NPs (Fig. S5a†) corresponded to the birnessite-layered manganese oxides (generally denoted as δ-MnO_2).[36] X-ray photoelectron spectroscopy (XPS) was used to study the valence state of Mn in the shell (Fig. S5b†). The binding energy of Mn $2p_{3/2}$ and $2p_{1/2}$ located at 642.0 and 653.8 eV was in good accordance with MnO_2 in the literature.[35] In Fig. S6,† no typical reduction peaks of Au on Au@MnO_2 NPs were detected by cyclic voltammograms (CV), indicating Au cores to be covered by MnO_2 shells without pinholes. In addition, no oxidation and reduction peaks were observed above 1.10 V, showing the structural stability of the MnO_2 substrate during the OER process.

Afterward, Ir was anchored on the MnO_2 shell using a simple and convenient method under ambient conditions. TEM showed the core–shell morphology of Au@MnO_2-IrO_x NPs (Fig. 1b). Scanning electron microscopy (SEM) showed good dispersion and no self-nucleated Ir particles (Fig. S7†). As shown in Fig. 1c, high-angle annular dark-field scanning transmission electron microscopy (HAADF-STEM) and energy dispersive X-ray spectroscopy (EDS) were conducted to elucidate the compositional distribution of the Au@MnO_2-IrO_x NPs, which showed that the inner cores were composed of the Au element that was surrounded by Mn and Ir, which were distributed across the outer shell. CV illustrated that the oxidation peak of Mn^{3+} to Mn^{4+} was still detected in Au@MnO_2-IrO_x NPs, suggesting an exposed MnO_2 surface (Fig. S6†). Owing to the influence of the large Au cores and thin oxide shells, Au@MnO_2-IrO_x-a NPs with a specific nanostructure were prepared (preparation and characterization details described in the ESI†) for characterization by HRTEM. As presented in Fig. 1d, the inner core delivered lattice spacings of 0.235 nm corresponding to Au (111). IrO_x clusters (0.223 nm) dispersed on the amorphous shell were also demonstrated. The surface chemical states of Mn and Ir were investigated by XPS as presented in Fig. 1e and f. The binding energy of Ir $4f_{7/2}$ and $4f_{5/2}$ of Au@MnO_2-IrO_x NPs was located at 61.4 and 64.4 eV, respectively, which were closed to +4 valence state and presented an upshift of 0.4 eV compared to the commercial Ir/C, indicating oxidized Ir valence state. The Mn 2p peaks led to a 0.3 eV downshift compared to Au@MnO_2 NPs. The shifts of the binding energy of both Ir 4f and Mn 2p indicated a strong electronic interaction with the charge transfer from IrO_x to MnO_2.

Rotating-disk-electrode measurements were carried out to evaluate the OER activity of Au@MnO_2-IrO_x, Au@Ir, Au@MnO_2 NPs, and commercial IrO_2 catalysts; the linear sweeping voltammograms (LSV) are shown in Fig. 2a. Au@MnO_2-IrO_x NPs required only 230 mV to achieve an OER current density of 10 mA cm^{-2}. In comparison, Au@Ir NPs and commercial IrO_2 catalysts displayed insufficient OER activities of 272 mV and 341 mV. Moreover, Au@MnO_2 NPs, as the substrate, showed poor OER activity. The electrochemical kinetics of these samples were demonstrated *via* Tafel plots based on the LSV curves in Fig. 2b. Au@MnO_2-IrO_x NPs delivered the lowest Tafel slope of 60 mV dec^{-1} showing faster kinetics than other tested catalysts. Moreover, the mass activities (M. A.) and turnover frequencies (TOF) at the overpotential of 300 mV were calculated to evaluate the intrinsic activities of catalysts (Fig. 2c). Au@MnO_2-IrO_x NPs presented mass activity and TOF of 4343 A g_{Ir}^{-1} and 2.16 O_2 s^{-1}, which were ~5.4 and 80 folds over Au@Ir NPs and IrO_2, respectively. The outstanding intrinsic activities were competitive among the reported OER electrocatalysts (Table S2†).

In Fig. 3a, *in situ* SERS was applied to investigate the MnO_2 substrate impacting the OER pathway of IrO_x centers. At 1.20 V, the spectra were mainly composed of the oxide signals between 400 and 800 cm^{-1}. The broad peak at ~597 cm^{-1} corresponded to the vibration mode of MnO_2, and the signals of IrO_x were covered because of lower content. When the potential increased to 1.25 V, the Raman peak at 751 cm^{-1} appeared and became stronger quickly as the potential rose until the maximum at ~1.45 V. On the other hand, another peak at ~1062 cm^{-1} was present at 1.40 V, which was the initial potential of OER, and gradually shifted to 1070 cm^{-1} at 1.70 V. *In situ* SERS of Au@MnO_2 NPs was carried out (Fig. S8†), and no peaks were detected at 700–1200 cm^{-1}, indicating that the species at 751 and 1062 cm^{-1} did not adsorb on the MnO_2 surface. To verify these two peaks, isotopic experiments were carried out. In the D_2O experiments (Fig. S9a†), no shifts were seen for these two peaks, proving that the species corresponding to them were irrelevant to the hydrogen atoms. For further verification, the solvent was replaced with $H_2{}^{18}O$ (Fig. S9b†). As presented in Fig. 3b, the peak at 1062 cm^{-1} shifted to 1004 cm^{-1} with the relative shift (frequency in $H_2{}^{18}O$/frequency in $H_2{}^{16}O$) of 94.5%, which was consistent with the theoretical relative shift of $*O–O^{-}$ of ~94.3% according to the mass formula.[29] Based on the theoretical model of the IrO_2 cluster loaded on the δ-MnO_2, DFT

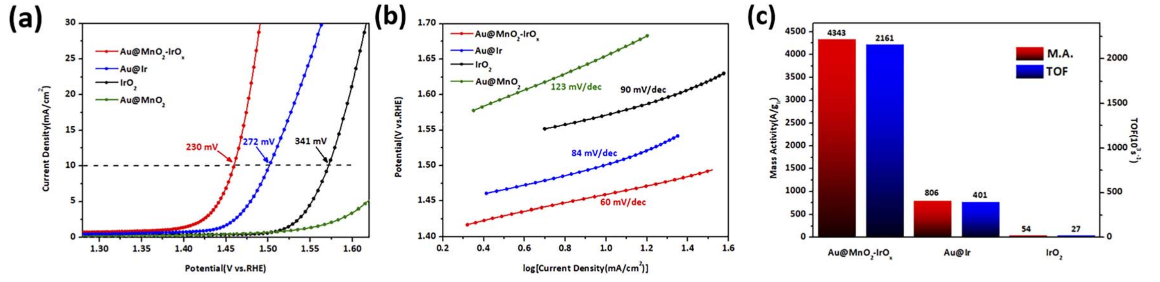

Fig. 2 (a) LSV polarization curves of Au@MnO_2-IrO_x, Au@Ir, Au@MnO_2 NPs, and commercial IrO_2. (b) Tafel plots of the above Ir catalysts corresponding to (a). (c) Mass activities and TOF of Ir catalysts corresponding to (a).

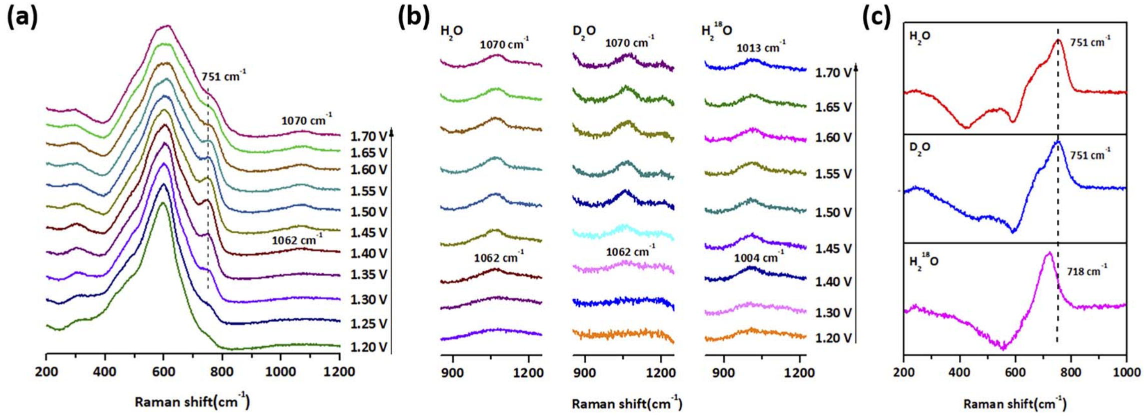

Fig. 3 (a) *In situ* electrochemical SERS of Au@MnO$_2$-IrO$_x$ NPs at 1.20–1.70 V (*vs.* RHE). (b) Isotopic Raman experiments of Au@MnO$_2$-IrO$_x$ NPs with the frequency range of ~1062 cm^{-1}. (c) Isotopic Raman experiments of Au@MnO$_2$-IrO$_x$ NPs with the frequency range between 200 and 1000 cm^{-1}. The subtractive spectra was performed by subtracting the spectra obtained at 1.20 V from the spectra at 1.40 V.

calculation was performed to demonstrate that the O–O stretching vibration of the *O–O$^-$ species delivered a theoretical wavenumber of 1042 cm^{-1}. The superoxide species have previously been detected by SERS, located at 1106 cm^{-1} on the Au (110) surface, 1142 and 1170 cm^{-1} on the NiFeO$_x$, and 1140–1180 cm^{-1} on the CoO$_x$.[37–39] As a result, the species located at 1062 cm^{-1} could be identified as the superoxide ion: *O–O$^-$, in our work. On the other hand, because of the overlap of the 751 cm^{-1} peak with the peaks of Mn and Ir oxides, a spectral subtraction was conducted to make the 751 cm^{-1} clearer (Fig. S10†). From the spectra processed in Fig. 3c, the 751 cm^{-1} shifted to 718 cm^{-1} in the H$_2{}^{18}$O solution, which indicated that the peak was related to species composed of only oxygen atoms. Wei and Liu reported the oxygen atom formed at Ir active sites with O-hetero-Ir-N$_4$ structures at 1.25 V, which was observed at 784 cm^{-1} by the SRIR analysis.[20] In addition, during the OER pathway, Ir–O species have been reported in the IrO$_x$/Au system and detected by *in situ* Raman spectroscopy to be located at 771 cm^{-1}.[40] DFT calculation also verified that the *O adsorbed on the IrO$_2$ crystal was located at 793 cm^{-1}. Therefore, 751 cm^{-1} in our system was identified as *O adsorbed on the IrO$_x$ centers.

For comparison, the OER pathway of Au@Ir NPs was detected by *in situ* SERS in Fig. 4a. At 1.20 V, the spectra originated from IrO$_2$ signals. As the potential increased to ~1.40 V, a peak arose at 749 cm^{-1} and became stronger gradually as the potential increased, which was also identified as the *O adsorbed on the Ir oxide. In addition, the peak at 455 cm^{-1} diminished, and peaks at 512 cm^{-1} and 592 cm^{-1} were enhanced. These transformations corresponded to the oxidation of IrO$_2$ from Ir^{4+} to Ir$^{4\cdot x+}$ in accordance with the spectroscopic results reported.[40,41] The oxidation behavior could also be verified by CV with the observation of an oxidation peak at 1.40 V (Fig. S12†). It is worth mentioning that the attenuation of 431 cm^{-1} ascribed to the oxidation of Ir^{4+} could be seen in the spectra of Au@MnO$_2$-IrO$_x$ after the spectral subtraction (Fig. S10†), and it appeared at 1.25 V coupled with the 751 cm^{-1} peak. According to some reported cases, promoting the formation of high valence Ir centers could favor the O–O coupling and improve the electrocatalytic activity.[42,43] Therefore, in our work, the oxidation of Ir^{4+} to the high valence state at a lower potential indicated the pre-activation of Ir oxide to promote the OER process.

As presented in Fig. 4b, the Raman intensity of peaks at 751 cm^{-1} and 1062 cm^{-1} in the Au@MnO$_2$-IrO$_x$ system and at 749 cm^{-1} in the Au@Ir system was normalized and related to the electrode potentials. Peak A arose at 1.25 V, and its intensity increased until 1.40 V, at which peak B appeared, and the OER on Au@MnO$_2$-IrO$_x$ occurred. On the other hand, the intensity of peak C scaled up from 1.40 V gradually with an increase in the potential. In short, Au@MnO$_2$-IrO$_x$ could adsorb *O at a lower potential even before the OER, and achieve saturation quickly, which facilitated the O–O coupling to form *O–O$^-$. However, Au@Ir adsorbed *O at the initial potential of OER and increased more slowly. In some reported works, modulating the dissociation of H$_2$O at reactive sites and metal–oxygen coupling was related to the reaction kinetics, and thus it impacted the OER activity.[44,45]

To further understand the connection between the absorption of *O and O–O coupling, Au@MnO$_2$-IrO$_x$-(b) NPs were prepared with a higher Ir loading for *in situ* SERS tests. In Fig. S13,† peaks at 458 cm^{-1} and 605 cm^{-1} corresponded to IrO$_2$ and MnO$_2$, respectively, referring to the above discussion. The strong Raman signal of IrO$_2$ indicated its abundance on the MnO$_2$ surface. Until the potential increased to 1.35 V, the oxidation of Ir^{4+} and adsorption of *O at 749 cm^{-1} occurred. At 1.40 V, the 1046 cm^{-1} peak corresponding to *O–O$^-$ appeared. As compared with the *O–O$^-$ species located at 1062 cm^{-1} on Au@MnO$_2$-IrO$_x$ NPs, lower Raman frequencies of O–O stretching vibration indicated a decline of O–O bond energy,[28] resulting in a higher energy barrier for O–O coupling.

DFT simulated reaction mechanism and the Gibbs free energy of intermediates on MnO$_2$–IrO$_2$ and IrO$_2$ were calculated in Fig. 4c. The model of MnO$_2$–IrO$_2$ was shown in Fig. S15,† where IrO$_2$ clusters were anchored on the δ-MnO$_2$. The energy barriers of O–O coupling and deprotonation of *OOH on MnO$_2$–IrO$_2$ were 1.68 and 1.62 eV, respectively, which was lower than 1.76 and 1.81 eV on the IrO$_2$ surface. Therefore, in Fig. 4b, as the

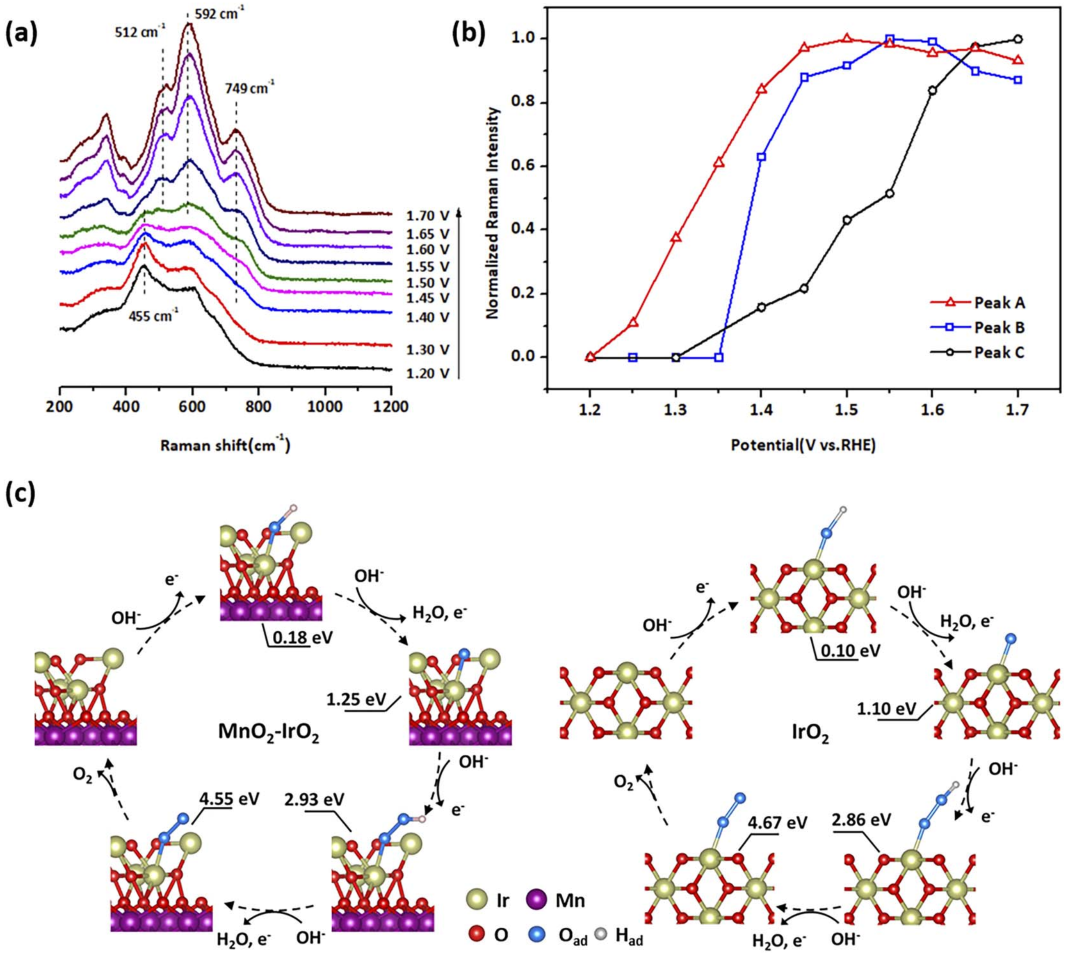

Fig. 4 (a) *In situ* electrochemical SERS of Au@Ir NPs at 1.20–1.70 V (*vs.* RHE). (b) Normalized Raman intensity of *O on the Au@MnO_2-IrO_x (Peak A), *O–O^- on the Au@MnO_2-IrO_x (Peak B), and *O on Au@Ir (Peak C) corresponding to the electrode potential. (c) DFT-calculated Gibbs free energies of OER pathways on MnO_2–IrO_2 and IrO_2.

OER occurred on the Au@Ir, the consumption of *O species was repressed by the O–O coupling step, inducing the accumulation of *O species on the surface with a gradual increase in the Raman signal of *O. However, as the OER started on the Au@MnO_2-IrO_x, *O species adsorbed before were consumed rapidly, and *O–O^- was concentrated on the surface, which resulted in a Raman signal of *O becoming stable and Raman signal of *O–O increasing immediately.

4. Conclusions

In summary, the Au@MnO_2-IrO_x catalysts, possessing the core–shell nanostructure of highly dispersed IrO_x clusters on the amorphous MnO_2 shells, were prepared using a simple and concise approach. Au@MnO_2-IrO_x NPs exhibited a low overpotential and extraordinary mass activity that outperformed traditional Ir catalysts. *In situ* SERS revealed the oxidation of Ir^{4+} and adsorption of *O on IrO_x centers at a low potential, which indicated the pre-activation of catalysts and facilitated the formation of the crucial OER intermediate: superoxide ion *O–O^-. The DFT calculations clarified the weakened energy barriers of O–O coupling and deprotonation of *OOH as compared to the IrO_2 surface, which was in good accordance with the results processed from Raman spectra. This work focuses on the mechanism of the impact of the substrate on the electrocatalytic behavior of Ir oxide, which may provide a new strategy for designing OER catalysts based on the SMSI.

Conflicts of interest

There are no conflicts to declare.

Acknowledgements

This work was supported by the National Key Research and Development Program of China (2020YFB1505800), the National Natural Science Foundation of China (21925404, 22104124, 22021001, and T2293692), and the Fundamental Research Funds for the Central Universities (20720220117).

References

1 Y. Jiao, Y. Zheng, M. Jaroniec and S. Z. Qiao, *Chem. Soc. Rev.*, 2015, **44**, 2060–2086.

2 N. T. Suen, S. F. Hung, Q. Quan, N. Zhang, Y. J. Xu and H. M. Chen, *Chem. Soc. Rev.*, 2017, **46**, 337–365.

3 J. Li, *Nano-Micro Lett.*, 2022, **14**, 112.

4 Z. F. Huang, J. Song, S. Dou, X. Li, J. Wang and X. Wang, *Matter*, 2019, **1**, 1494–1518.

5 J. Song, C. Wei, Z. F. Huang, C. Liu, L. Zeng, X. Wang and Z. J. Xu, *Chem. Soc. Rev.*, 2020, **49**, 2196–2214.

6 Y. Lee, J. Suntivich, K. J. May, E. E. Perry and Y. Shao-Horn, *J. Phys. Chem. Lett.*, 2012, **3**, 399–404.

7 Y. Yao, S. Hu, W. Chen, Z. Q. Huang, W. Wei, T. Yao, R. Liu, K. Zang, X. Wang, G. Wu, W. Yuan, T. Yuan, B. Zhu, W. Liu, Z. Li, D. He, Z. Xue, Y. Wang, X. Zheng, J. Dong, C. R. Chang, Y. Chen, X. Hong, J. Luo, S. Wei, W. X. Li, P. Strasser, Y. Wu and Y. Li, *Nat. Catal.*, 2019, **2**, 304–313.

8 R. Frydendal, E. A. Paoli, B. P. Knudsen, B. Wickman, P. Malacrida, I. E. L. Stephens and I. Chorkendorff, *ChemElectroChem*, 2014, **1**, 2075–2081.

9 H. Wu, Y. Wang, Z. Shi, X. Wang, J. Yang, M. Xiao, J. Ge, W. Xing and C. Liu, *J. Mater. Chem. A*, 2022, **10**, 13170–13189.

10 J. Shan, T. Ling, K. Davey, Y. Zheng and S. Z. Qiao, *Adv. Mater.*, 2019, **31**, 1900510.

11 H. Wang, Z. N. Chen, D. Wu, M. Cao, F. Sun, H. Zhang, H. You, W. Zhuang and R. Cao, *J. Am. Chem. Soc.*, 2021, **143**, 4639–4645.

12 S. Hao, H. Sheng, M. Liu, J. Huang, G. Zheng, F. Zhang, X. Liu, Z. Su, J. Hu, Y. Qian, L. Zhou, Y. He, B. Song, L. Lei, X. Zhang and S. Jin, *Nat. Nanotechnol.*, 2021, **16**, 1371–1377.

13 Y. Zhang, X. Zhu, G. Zhang, P. Shi and A. L. Wang, *J. Mater. Chem. A*, 2021, **9**, 5890–5914.

14 L. Liu and A. Corma, *Chem. Rev.*, 2018, **118**, 4981–5079.

15 Z. Luo, G. Zhao, H. Pan and W. Sun, *Adv. Energy Mater.*, 2022, **12**, 2201395.

16 Y. Mu, T. Wang, J. Zhang, C. Meng, Y. Zhang and Z. Kou, *Electrochem. Energy Rev.*, 2021, **5**, 145–186.

17 Q. Zhang, Z. Duan, Y. Wang, L. Li, B. Nan and J. Guan, *J. Mater. Chem. A*, 2020, **8**, 19665–19673.

18 H. He, J. Chen, D. Zhang, F. Li, X. Chen, Y. Chen, L. Bian, Q. Wang, P. Duan, Z. Wen and X. Lv, *ACS Catal.*, 2018, **8**, 6617–6626.

19 X. Zheng, M. Qin, S. Ma, Y. Chen, H. Ning, R. Yang, S. Mao and Y. Wang, *Adv. Sci.*, 2022, **9**, 2104636.

20 H. Su, W. Zhou, W. Zhou, Y. Li, L. Zheng, H. Zhang, M. Liu, X. Zhang, X. Sun, Y. Xu, F. Hu, J. Zhang, T. Hu, Q. Liu and S. Wei, *Nat. Commun.*, 2021, **12**, 6118.

21 Z. Shi, Y. Wang, J. Li, X. Wang, Y. Wang, Y. Li, W. Xu, Z. Jiang, C. Liu, W. Xing and J. Ge, *Joule*, 2021, **5**, 2164–2176.

22 C. Lin, J. L. Li, X. Li, S. Yang, W. Luo, Y. Zhang, S.-H. Kim, D.-H. Kim, S. S. Shinde, Y.-F. Li, Z. P. Liu, Z. Jiang and J. H. Lee, *Nat. Catal.*, 2021, **4**, 1012–1023.

23 Y. Qin, Y. Liu, Y. Zhang, Y. Gu, Y. Lian, Y. Su, J. Hu, X. Zhao, Y. Peng, K. Feng, J. Zhong, M. H. Rummeli and Z. Deng, *ACS Catal.*, 2022, **13**, 256–266.

24 R. Panneerselvam, G. K. Liu, Y. H. Wang, J. Y. Liu, S. Y. Ding, J. F. Li, D. Y. Wu and Z. Q. Tian, *Chem. Commun.*, 2017, **54**, 10–25.

25 J. F. Li, Y. J. Zhang, S. Y. Ding, R. Panneerselvam and Z. Q. Tian, *Chem. Rev.*, 2017, **117**, 5002–5069.

26 Z. Q. Tian, B. Ren, J. F. Li and Z. L. Yang, *Chem. Commun.*, 2007, **34**, 3514–3534.

27 Y. J. Zhang, P. M. Radjenovic, X. S. Zhou, H. Zhang, J. L. Yao and J. F. Li, *Adv. Mater.*, 2021, **33**, 2005900.

28 H. Ze, X. Chen, X. T. Wang, Y. H. Wang, Q. Q. Chen, J. S. Lin, Y. J. Zhang, X. G. Zhang, Z. Q. Tian and J. F. Li, *J. Am. Chem. Soc.*, 2021, **143**, 1318–1322.

29 J. C. Dong, X. G. Zhang, V. Briega-Martos, X. Jin, J. Yang, S. Chen, Z. L. Yang, D. Y. Wu, J. M. Feliu, C. T. Williams, Z. Q. Tian and J. F. Li, *Nat. Energy*, 2018, **4**, 60–67.

30 Y. H. Wang, J. B. Le, W. Q. Li, J. Wei, P. M. Radjenovic, H. Zhang, X. S. Zhou, J. Cheng, Z. Q. Tian and J. F. Li, *Angew. Chem., Int. Ed.*, 2019, **58**, 16062–16066.

31 A. Moysiadou, S. Lee, C. S. Hsu, H. M. Chen and X. Hu, *J. Am. Chem. Soc.*, 2020, **142**, 11901–11914.

32 O. Diaz-Morales, D. Ferrus-Suspedra and M. T. M. Koper, *Chem. Sci.*, 2016, **7**, 2639–2645.

33 L. Lu, G. Sun, H. Zhang, H. Wang, S. Xi, J. Hu, Z. Tian and R. Chen, *J. Mater. Chem.*, 2004, **14**, 1005–1009.

34 G. Frens, *Nat. Phys. Sci.*, 1973, **241**, 20–22.

35 X. D. Lin, V. Uzayisenga, J. F. Li, P. P. Fang, D. Y. Wu, B. Ren and Z. Q. Tian, *J. Raman Spectrosc.*, 2012, **43**, 40–45.

36 D. Chen, D. Ding, X. Li, G. H. Waller, X. Xiong, M. A. El-Sayed and M. Liu, *Chem. Mater.*, 2015, **27**, 6608–6619.

37 C. Hu, Y. Hu, C. Fan, L. Yang, Y. Zhang, H. Li and W. Xie, *Angew. Chem., Int. Ed.*, 2021, **60**, 19774–19778.

38 J. Zhang, X. G. Zhang, J. C. Dong, P. M. Radjenovic, D. J. Young, J. L. Yao, Y. X. Yuan, Z. Q. Tian and J. F. Li, *J. Am. Chem. Soc.*, 2021, **143**, 20049–20054.

39 Y. Hu, C. Hu, A. Du, T. Xiao, L. Yu, C. Yang and W. Xie, *Anal. Chem.*, 2023, **95**, 1703–1709.

40 Z. Pavlovic, C. Ranjan, M. van Gastel and R. Schlögl, *Chem. Commun.*, 2017, **53**, 12414–12417.

41 K. H. Saeed, M. Forster, J. F. Li, L. J. Hardwick and A. J. Cowan, *Chem. Commun.*, 2020, **56**, 1129–1132.

42 Y. Qin, Z. Wang, W. Yu, Y. Sun, D. Wang, J. Lai, S. Guo and L. Wang, *Nano Lett.*, 2021, **21**, 5774–5781.

43 Q. He, S. Qiao, Q. Zhou, Y. Zhou, H. Shou, P. Zhang, W. Xu, D. Liu, S. Chen, X. Wu and L. Song, *Nano Lett.*, 2022, **22**, 3832–3839.

44 N. Wang, Z. Cao, X. Zheng, B. Zhang, S. M. Kozlov, P. Chen, C. Zou, X. Kong, Y. Wen, M. Liu, Y. Zhou, C. T. Dinh, L. Zheng, H. Peng, Y. Zhao, L. Cavallo, X. Zhang and E. H. Sargent, *Adv. Mater.*, 2020, **32**, 1906806.

45 C. Cai, K. Liu, L. Zhang, F. Li, Y. Tan, P. Li, Y. Wang, M. Wang, Z. Feng, D. Motta Meira, W. Qu, A. Stefancu, W. Li, H. Li, J. Fu, H. Wang, D. Zhang, E. Cortes and M. Liu, *Angew. Chem., Int. Ed.*, 2023, e202300873, DOI: 10.1002/anie.202300873.